C. R. Mecanique 344 (2016) 167–180

Contents lists available at ScienceDirect

Comptes Rendus Mecanique

www.sciencedirect.com

Aspect ratio of undulation in a vertically vibrated granular layer

Yoshihito Dose [a], Osamu Sano [b,*,1]

[a] Department of Applied Physics, Tokyo University of Agriculture and Technology, Koganei, Tokyo 184-8588, Japan
[b] Tokyo University of Agriculture and Technology, Fuchu, Tokyo 183-8538, Japan

ARTICLE INFO

Article history:
Received 3 June 2015
Accepted 4 November 2015
Available online 3 February 2016

Keywords:
Granular material
Vertical vibration
Undulation
Aspect ratio
Eigenmode
Buckling

ABSTRACT

The aspect ratio of the height δ to the wavelength λ of the undulation generated by a vertical vibration of the granular layer was investigated experimentally, and its dependence on the frequency f and amplitude a is disclosed. We found that δ/λ is well described by an almost linear function of fa rather than by that of $\Gamma \equiv (2\pi f)^2 a/g$, irrespective of the horizontal size of the container, where g is the acceleration of gravity. Appearance of sub-arches to maintain the main eigenmode and the transitions between eigenmodes of undulation are also elucidated.

1. Introduction

Vertically vibrated granular layer confined in a vessel shows typical wave motions depending on the amplitude a and frequency f of the external forcing [1–5]. In addition to the planar pattern [6–12] or cross-sectional pattern [13–19] of *ripples*, the cross-sectional structures on the vibrated granular layers, such as the regular pattern of defects [20], transverse bending [21], arches [22], and kinks [23] have been reported. In contrast to the ripples, the latter patterns have common features of wavy deformations characterized by arch-like *undulation* of an almost constant thickness layer with integer or half-integer number of waves along the layer, and alternating ridge-foot positions with a period twice of the forcing period. The onset of the undulation, or the regular pattern of defects, was investigated as early as 1989 by Douady et al. [20]. They proposed a relation between the minimum distance l between "solidified parts" of the layer normalized by the layer thickness h (as shown in Fig. 1) and the non-dimensional acceleration $\Gamma \equiv (2\pi f)^2 a/g$ (f and a are the frequency and amplitude of external oscillation, and g is the acceleration of gravity) described by

$$\frac{h}{l} \approx 0.16(\Gamma - 4.2) \tag{1}$$

We have performed an essentially similar experiment using an experimental apparatus, the details of which have been given in our previous papers [24–26]. A rectangular container made of a transparent acrylic resin with horizontal dimensions $L \times W$ ($W \ll L$) and height H was mounted vertically on an electromagnetic shaker. The container was oscillated sinusoidally with a frequency f and an amplitude a, so that the position of the container bottom z is given by $z = a\sin(2\pi f t)$. Here

* Corresponding author.
E-mail address: sano@cc.tuat.ac.jp (O. Sano).
[1] Professor Emeritus.

http://dx.doi.org/10.1016/j.crme.2015.11.005
1631-0721/

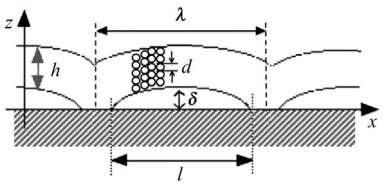

Fig. 1. Definition sketch of undulation.

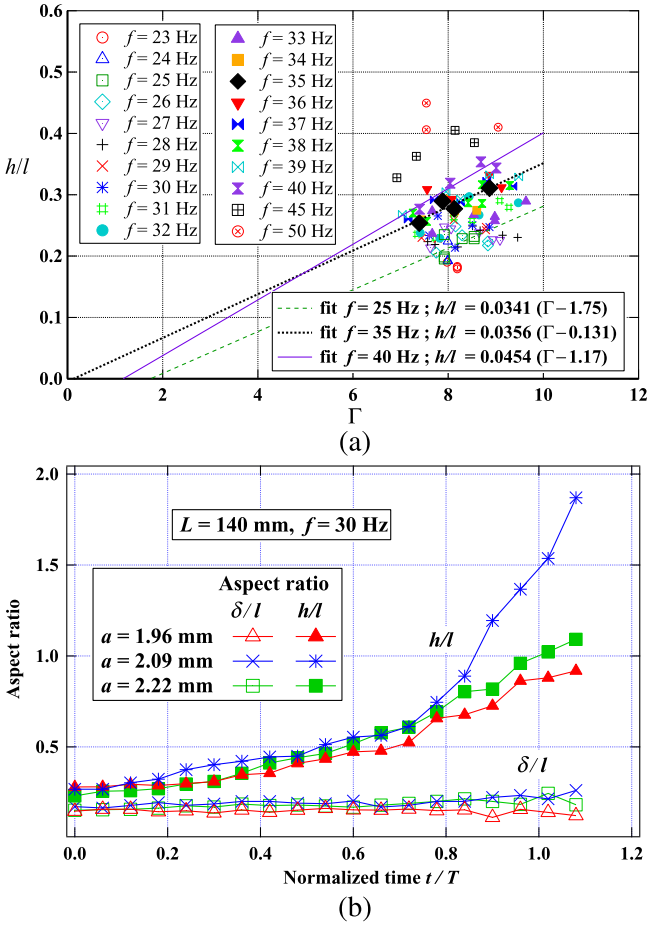

Fig. 2. (a) Dependence of h/l on Γ, and (b) time variation of h/l and δ/l. For the definition of h, l and δ, see the text and Fig. 1. All the data are due to the measurement of the undulation presented in this paper, which may not be appropriately described by a single linear fit in terms of Γ.

we have taken the Cartesian coordinate axes x and z in the horizontal and vertical directions, respectively. The pattern formation of a vertically oscillated layer of granular material of a prescribed thickness h consisting of about ten layers of spherical particles was observed from the side by a high-speed video camera.

We show in Fig. 2(a) the relation of the ratio h/l to the non-dimensional acceleration Γ as was described by Douady et al. [20], where all of the plotted data are the ones obtained in our experiment. In spite of larger scattering, an almost linear relation is recognized for respective frequencies f, which seems to confirm the results of Douady et al. [20]. The slopes and the critical Γ of the fitting curves, however, vary between different sets of external forcing. We also show the time variation of h/l for a particular case in Fig. 2(b). The abscissa is the time normalized by the period of oscillation T, where the time $t = 0$ is chosen when the container's wall is at the lowest position. As has been expected, the horizontal extension l varies with time between 0 and a certain length (of the order of the container size), while the layer thickness is almost constant, so that the ratio h/l varies considerably. This raises a question on the timing of measurement of the arch structure. On the other hand, the ratio δ/l remains almost constant as is shown in Fig. 2(b), where δ is the height of the arch. These results imply that the original Douady plot may not be a universal relation, and/or the characteristic lengths ratio h/l, and Γ may not be appropriate parameters.

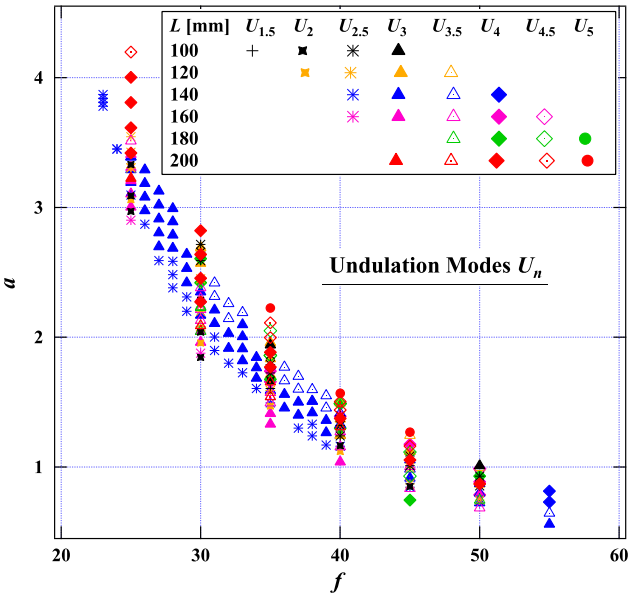

Fig. 3. Frequency f and amplitude a of the external forcing, in which the undulations are reported in the present paper. U_n refers the eigenmode of the granular layer confined in a container of horizontal size L, where n (being an integer or a half integer) is the number of waves of the bending motion of the layer.

The importance of the particle velocity v or fa, instead of Γ, on the characterization of the vertically oscillated granular layer has already been pointed out. For instance, Umbanhowar and Swinney [12] deals with the square/stripe patterns, and proposed the different wavelength scaling depending on the extent of "grain mobility" $\tilde{v}_{\rm gm} \equiv 2\pi af/\sqrt{gd}$, which reflects solid–fluid transition. The scaling of dilatation and meltdown of the granular layer using the container velocity v_0 ($\propto fa$) rather than acceleration Γ has also been pointed out by Götzendorfer et al. [27]. In the latter, the center of mass of the vibrating granular layer is plotted against v_0 and is compared with the one scaled by Γ. They used different materials with selected frequencies of oscillation, and varied the oscillation amplitude in more detail. Their data show a larger scattering in the Γ plot, while better fitting by the v_0 plot is obtained. The latter, however, deals with fluidization, so that no structure formation such as ripples or undulation is mentioned. We have also remarked the importance of momentum transfer ($\propto fa$) for characterizing *ripples* in the vertically vibrated granular layer [16–19], which suggests a similar essential role in the formation of *undulation*.

So far the formation mechanism of undulation has been examined in detail [24–26], in which the buckling due to the dilatancy of the layer at the collision with the bottom wall is found to be the fundamental mechanism. Here, the horizontally dilated layer due to the impact on the container's bottom wall is forced to bend so as to adjust the elongated length of the layer, which is reminiscent of the buckling and bending of the elastic plate [28]. The characteristics of undulation, however, are not yet fully understood. For instance, what determines the number of undulation waves n, or what determines the structure of undulation such as δ and λ? Obviously they will depend on the material properties of the particle, such as the diameter, the density, the friction constant, and the restitution coefficient, etc., as well as the magnitude of external forcing (f and a). It will also depend on the thickness h and on the horizontal size of the container L. The latter is included here as a control parameter, because the number of waves n, and hence the mode, is likely to increase with the increase in L, if other conditions to realize a particular undulation mode are the same. To avoid the complexity, we shall consider in this paper a single species of granular material of a fixed size and an otherwise fixed layer thickness, and focus our attention on the dependence of the undulation's characteristics on the external forcing conditions (f and a) and the container size L.

2. Experiment

We observed an undulation of about 10 layers of lead spheres of a diameter $d = 1.09 \pm 0.09$ mm filled in a container of horizontal dimension $L = 100{\sim}200$ mm, height $H = 90$ mm and width $W = 5$ mm. All the measurements were made after the stationary states of undulation were reached under atmospheric pressure. In our previous researches [24–26], the type of undulation with n arches of undulation (n being integers) is denoted by S_n, whereas the type with $n - 1/2$ arches by A_n. In the following, we denote both types by U_n, where n is an integer or a half integer.

Fig. 3 is the f–a diagram, where some types of eigenmodes of undulation are recognized. Generally speaking, higher eigenmodes appear for larger f and/or larger a. An overlap of the region of undulation modes for different container sizes is recognized.

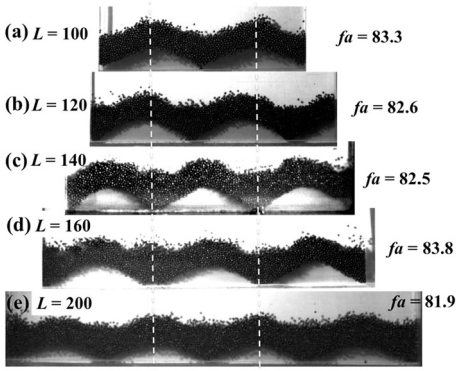

Fig. 4. Undulations observed in the container of different sizes. Comparison of the wavelength under external forcing with almost the same fa. (a) U_2, (b) $U_{2.5}$, (c) and (d) U_3, (e) U_4 mode.

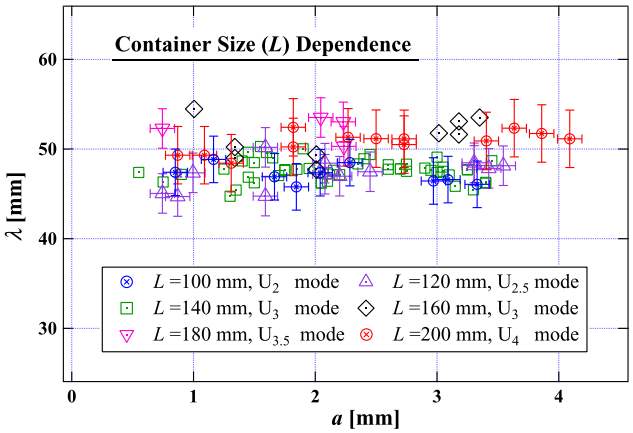

Fig. 5. Comparison of undulation modes in the container of different sizes, where the combination of f and a is varied. Error bars are omitted for $L =$ 140 mm and 160 mm cases in order to avoid the overlapping of data points, but they are almost the same as those in other cases.

2.1. Container size dependence of the wavelength of the eigenmode

As has been mentioned, undulation is interpreted as eigenmodes of buckling of the granular layer. This naturally raises a question on the dependence of the container size on the wavelength. In order to clarify the latter, we performed experiments using a container of varied horizontal sizes, and compared the wavelengths of undulation. Fig. 4 is an example showing the dependence of the container size L on the undulation wavelength λ. These waves are realized under conditions that are close to eigenmodes in a given container. We can recognize the agreement between λ of the U_2 mode in $L = 100$ mm (Fig. 4(a)) and λ of the U_4 mode in $L = 200$ mm (Fig. 4(e)) within the experimental accuracy. Fig. 5 compares the conditions under which such a wave is observed in a container of different sizes, where the combination of f and a is varied so that a stable state is reached. The ordinate is the wavelength, whereas the abscissa is the amplitude of external forcing a. As far as the near eigenmode is concerned, the wavelength under the same fa values looks almost the same irrespective of the container size L, so that the number of waves n of the eigenmode U_n is proportional to L (in expectation of $n = L/\lambda$). In view of the exact eigenvalue problem for the buckling of a continuum elastic plate, the container size L required for $U_{2.5}$ is 125 mm, which looks nearly satisfied in the $L = 120$ mm case (Fig. 4(b)). Similarly, the U_3 mode requires $L = 150$ mm, which is marginally satisfied in the $L = 140$ mm case (Fig. 4(c) and $L = 160$ mm case (Fig. 4(d)). The latter two cases, however, suggest that the eigenvalue problem of the granular layer is not completely determined by the relation $n = L/\lambda$. The wavelengths in Fig. 4(c) and (d) are slightly modified to adjust the container size, which will be checked in detail in the next subsections.

2.2. Adjusting zone

In contrast to the buckling of a continuum elastic plate, where every eigenmode requires a well-defined wavelength L/n, wider variations of the wavelength are recognized in the undulation of a granular layer. A closer look of our observation reveals that the solidified part of the granular layer seems to play a role of effective boundary to form the foot of the arch, which relaxes the eigenvalue conditions on the container size L as well as the forcing conditions on f and a. Examples

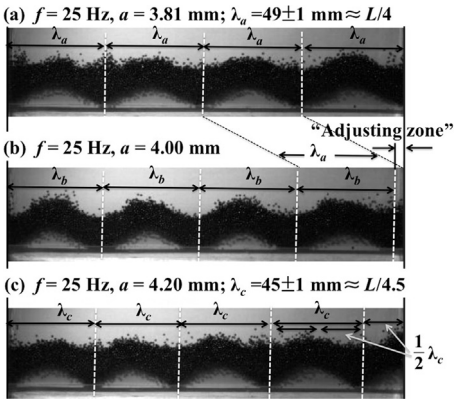

Fig. 6. Typical undulations observed at the maximum amplitude of the arches ($L = 200$ mm, $f = 25$ Hz): (a) U_4 mode, (b) U_4 mode with the adjusting zone, and (c) $U_{4.5}$ mode.

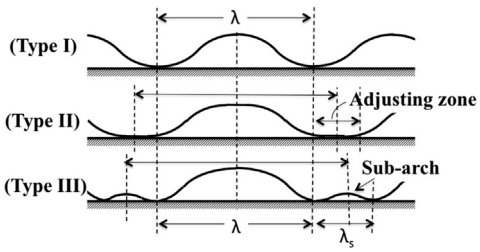

Fig. 7. Type of wavelength adjustment. Type I corresponds to one of the eigenmodes. Type II admits the part of the layer in contact with the bottom wall elongated and flattened so as to adjust the eigenmode condition. Sub-arches appear in Type III, which also adjust the eigenmode condition.

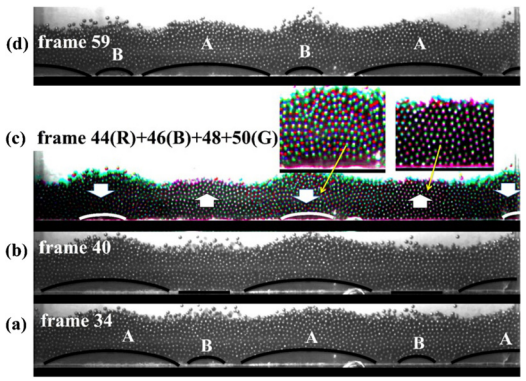

Fig. 8. Undulations accompanied by the formation of sub-arches ($U_{2.5}$ mode under $f = 39$ Hz, $a = 1.17$ mm in a container of $L = 140$ mm). (a) Main arches denoted by "A" and sub-arches denoted by "B" at $t = 0$ (frame 34), (b) sub-arches disappear (frame 40), (c) four pictures at frames 44 (red), 46 (blue), 48 (gray) and 50 (green) are superposed, which describe the direction of motion of particles shown by arrows, and (d) main arches and sub-arches at $t \approx T$ (frame 59). (For interpretation of the references to color in this figure legend, the reader is referred to the web version of this article.)

of such snapshots are shown in Fig. 6, all of which are observed at the maximum amplitude of arches of the layer in the container $L = 200$ mm under $f = 25$ Hz. The U_4 mode is observed at (a) $a = 3.81$ mm and (b) $a = 4.00$ mm, where an adjusting zone adjacent to the right side wall is recognized in the latter. Here, an "adjusting zone" is the part of the layer where the granular material is immobilized and bridges both ends of the waves (as illustrated by Type II in Fig. 7). With the increase of external forcing, the adjustment is no longer accomplished and a higher mode $U_{4.5}$ appears in (c) $a = 4.20$ mm.

2.3. Sub-arches for adjustment

The adjustment shown in the previous subsection is mainly observed near the side walls of the container. A closer look at the experimental findings reveals the appearance of sub-arches as is illustrated by Type III in Fig. 7. These sub-arches are probably the same as the ones described by Douady et al. [20], but the latter did not deal with in detail. Typical example of the Type-III undulation is shown in Fig. 8, which is obtained at $f = 39$ Hz, $a = 1.17$ mm in the container $L = 140$ mm. The

container's bottom wall is at the lowest position at phase (a) (frame 34, $t = 0$), whereas it is at the highest position at phase (d) (frame 59, $t \approx T$). In both cases, arches of two different sizes, the main arches of wavelength λ and the sub-arches of wavelength λ_s, denoted by "A" and "B", respectively, in Fig. 8 are recognized. As the container's bottom is pushed up, while the granular layer is almost in a stationary state, these arches decrease their heights, so that the sub-arches "B" disappear in (b). Fig. 8(c) shows the subsequent movement of particles. In the latter, four pictures at frames 44 (red), 46 (blue), 48 (gray) and 50 (green) are superposed (the frame rate being one frame per one millisecond). The main arches in Fig. 8(a) and (b) become smaller in size but do not disappear because of the bridging associated with volume exclusion. On the other hand, the flat regions in Fig. 8(b), where sub-arches were previously observed, are compressed and yield buckling, so that these parts give rise to convex bending, and develop into the main arches in phase (d) ($t \approx T$). Here, the sub-arches (previously the main arches, which decrease in size and are solidified) serve as the effective boundaries for the main arches. The processes from (a) to (d) are repeated with the positions of main arches and sub-arches alternating with each other, so that the same pattern is reproduced after $t = 2T$.

2.4. Eigenmode transition

We have shown that in a container of a given size, higher eigenmodes appear with the increase of external forcing fa. In contrast to the buckling of the plate of a continuum medium, where sharp transitions between eigenmodes occur, eigenmode transitions in the granular layer are not so sharp due to the appearance of adjusting zones (Fig. 7).

Figs. 9(a)–(c) show examples of mode transition from U_n to $U_{n+1/2}$, where n is an integer or a half-integer. The abscissa is the amplitude of forcing fa, whereas the ordinate is the difference $\delta L (\equiv L - n\lambda)$ normalized by the exact wavelength $\lambda_e (\equiv L/n)$ of the relevant eigenmode. The solid lines connect the states in the same mode through an adjustment of Type II (Fig. 7), whereas the broken lines correspond to the mode transitions. When $\delta L/\lambda_e$ exceeds a certain amount, presumably 0.1 or larger, a transition of mode U_n to mode $U_{n+1/2}$ may be invoked. Physical processes of these transitions are illustrated by Fig. 10. In the exact eigenstate, either in $U_{n-1/2}$ or U_n mode, δL is zero (see Fig. 10(b) and (e)). When the wavelength decreases in the former, δL becomes positive (Fig. 10(c)). With further decrease in the wavelength, almost one half wave of the undulation is recognized (as described in Fig. 10(d)), so that a transition of mode $U_{n-1/2}$ to mode U_n is admitted. The container, however, does not have sufficient space to allow a whole wave, so that $\delta L < 0$ at this stage (Fig. 10(d)). This type of transition from Fig. 10(c) to (d) was most frequently observed in our experiment, which we refer to as "Mode transition (I)" as is shown in Fig. 9(a). The mode transitions from (a) to (f) ("Mode transition (II)"), and the mode transitions from (a) to (d) ("Mode transition (III)") were also observed as shown in Fig. 9(b) and (c), respectively. Other possible types of mode transition from (c) to (f) ("Mode transition (IV)") was not observed in our present experiment.

2.5. Spatiotemporal behavior of undulation

We have ascribed the undulation to the buckling and bending of the granular layer due to the dilatancy of the layer at the impact of the container wall. The layer, of course, deforms dynamically both in space and time, so that a question arises at what phase of oscillation the structure of undulation is best characterized.

We show the illustrative space–time diagram of the contour of the "ideal" undulation in Fig. 11, where the amplitude of the oscillation of the container's bottom wall is neglected. The abscissa is the horizontal position of the lower boundary of the granular layer extending two wavelengths (U_2 case) and the ordinate is the time that covers a half cycle of undulation $T (\equiv 1/f)$. The initial "arch" of the layer decreases its width and height, becomes flat (but the layer itself is dilated) at time $t = T/2$, and new arches emerge at positions that are formerly valley regions. An example of experimental data, observed under $f = 32$ Hz, $a = 2.26$ mm in the container $L = 140$ mm, is shown in Fig. 12, which basically agrees with the ideal case shown in Fig. 11. A closer look of the experimental data, however, reveals some differences. At $t \approx T/2$, the layer is almost flat, so that the void space between the grains and the space below the arches is indistinguishable, which blurs the boundary of arches. Moreover, a finite-amplitude vertical displacement of the container wall as well as the volume exclusion of particles induces the change of positions of the foots of arches sideways differently depending on the phase of collisions, which reflects the fore-and-aft asymmetry of the diagram at $t \approx T/2$.

Fig. 13(a) illustrates the "ideal" spatiotemporal diagram of the Type III, where the amplitude of the oscillation of the container's bottom wall is neglected. The contours of the lower boundary at typical timings are illustrated by thick solid lines. The broken lines describe the positions of the layer that are in contact with the container's wall. The regions marked by "A" and "B" correspond to the main arches and sub-arches, respectively. An example of the space–time diagram of Type III undulation is shown in Fig. 13(b), which corresponds to the one described in Fig. 8. Main arches and sub-arches are also denoted by "A" and "B", respectively, which alternate periodically both in space and time. In the region denoted by "C", the void space between the grains and the space below the arches is indistinguishable in our experiment.

2.6. Aspect ratio of arch height to wavelength

In order to characterize the arch structure, we have measured the *maximum height* of the arch δ and the wavelength λ. Taking into account the adjusting zones and/or sub-arches stated in the previous subsections, we restrict our attention to the aspect ratios of the undulations in near eigenmodes. Fig. 14 is the result obtained in a container of $L = 140$ mm, where

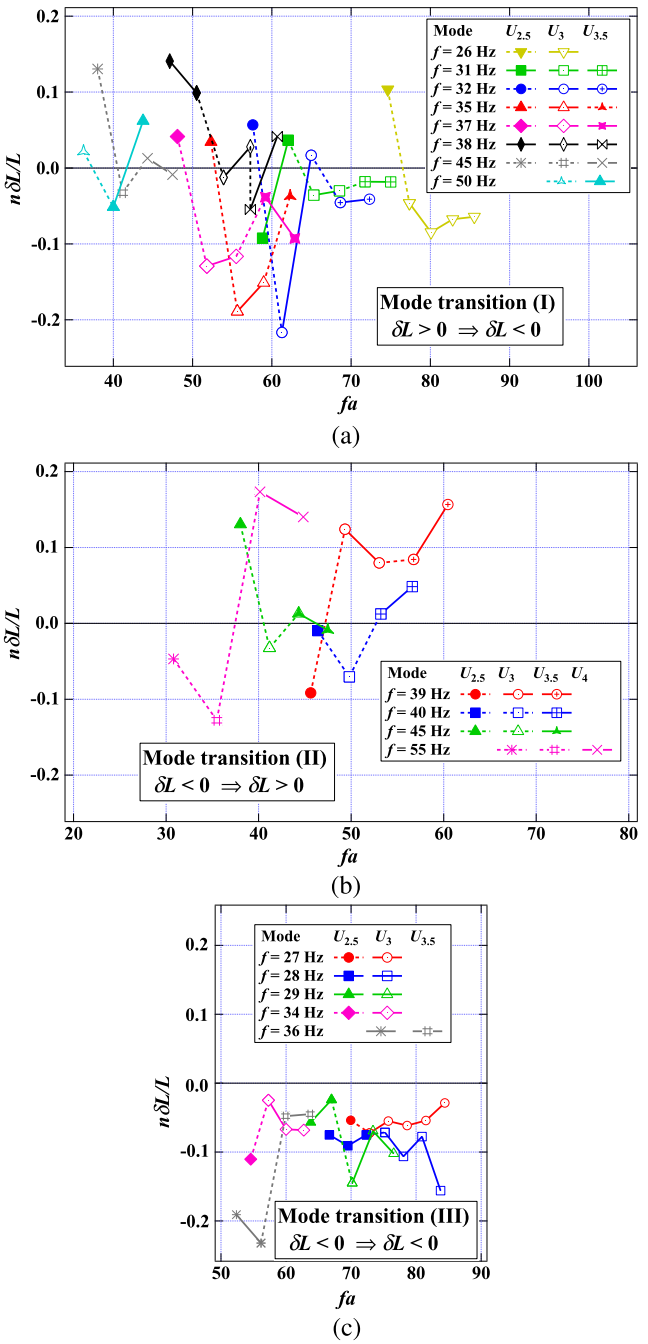

Fig. 9. Adjustment of the wavelength and the mode transition observed in the container $L = 140$ mm. The ordinate is the difference of the observed wavelength normalized by the exact wavelength, whereas the abscissa is the amplitude of forcing (proportional to fa). The broken lines show the transition of the mode from U_n to $U_{n+1/2}$, where n is an integer or a half integer.

the ordinate is δ/λ. We adopted λ rather than l for normalizing the height δ to avoid the ambiguity of determining the accurate positions of the foot of the arch that are dynamically compacted. The abscissa of Fig. 14(a) is Γ, whereas that of Fig. 14(b) is fa. The former plots show that undulations appear in the Γ range between 6 and 10, but the data points are broadly distributed, which suggests that the scaling in terms of Γ is not necessarily appropriate. On the other hand, rather good fitting of δ/λ against fa is given by

$$\frac{\delta}{\lambda} = 0.00365\,(fa - 20.5) \tag{2}$$

which suggests that the aspect ratio of the arch is well described by fa.

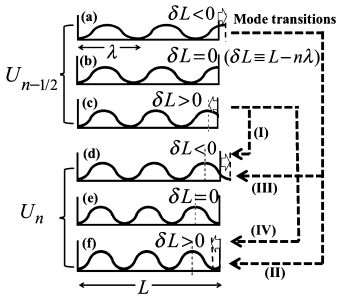

Fig. 10. Illustration of the type of mode transitions. With the decrease of the wavelength, the mode $U_{n-1/2}$ with $\delta L > 0$ easily exhibits a transition to U_n with $\delta L < 0$, as is described by transition mode (I) in the figure, where $\delta L \equiv L - n\lambda$.

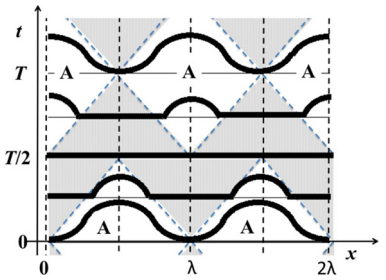

Fig. 11. Space–time diagram of the "ideal" undulation, where the amplitude of the oscillation of the container's bottom wall is neglected. Contours of the lower boundary of the granular layer at typical timings are illustrated by thick solid lines. The broken lines describe the positions of the layer that are in contact with the container wall. The regions marked "A" correspond to the arch. Peak and valley regions alternate periodically in space and time.

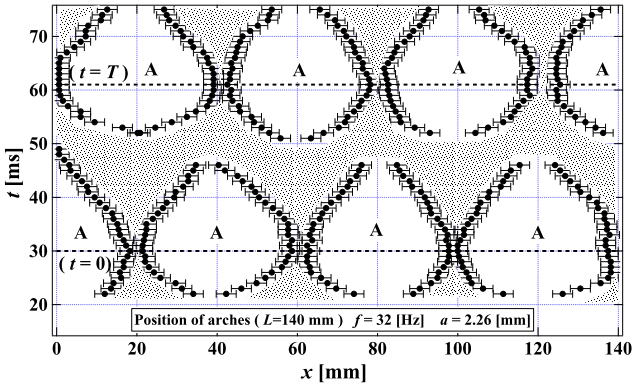

Fig. 12. An example of the space–time diagram of the undulating layer ($L = 140$ mm, $f = 32$ Hz, $a = 2.26$ mm). Periodic alternations of the peak and valley regions are recognized, but the boundaries of the arches are blurred because of the finite size of particles as well as the finite amplitude of the oscillation of the bottom wall.

Fig. 15 shows the aspect ratios δ/λ similarly obtained in a container of various sizes. The abscissa of Fig. 15(a) is Γ, whereas that of Fig. 15(b) is fa. In spite of some scattering, all the data seem to be well described by a line in the latter. Fig. 15(c) shows the dependence of the slopes and critical values giving the best fits of the data by a line

$$\frac{\delta}{\lambda} = \alpha\,[fa - (fa)_c] \tag{3}$$

which suggests that the aspect ratio of arch height to wavelength is similarly described by fa irrespective of the container size.

3. Conclusion

We have experimentally investigated the undulation of the granular layer in a container of various horizontal dimensions L, which is sinusoidally vibrated vertically with frequency f and amplitude a. Our findings are as follows.
(i) We have confirmed that the undulation is due to the buckling of the granular layer by the lateral force associated with the dilatancy generated by the impact of the layer on the container wall. A higher eigenmode U_n, whose number of

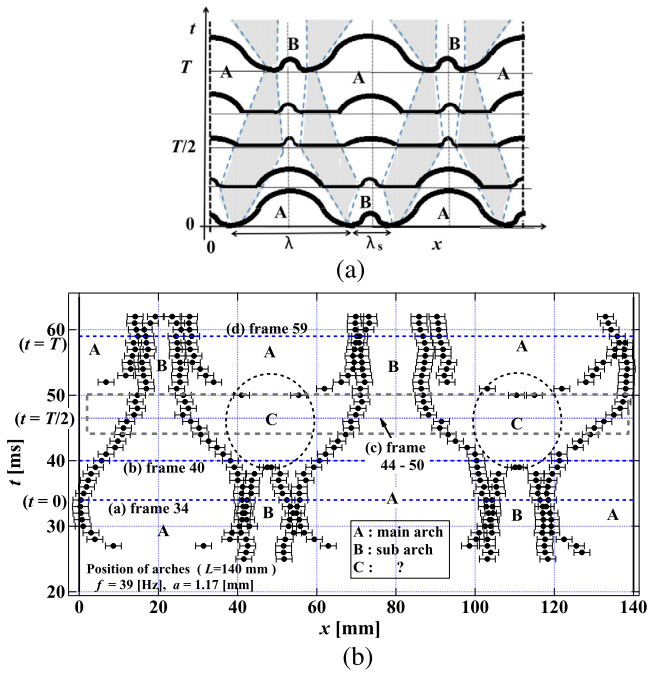

Fig. 13. (a) Space–time diagram of the "ideal" Type-III undulation, where the amplitude of the oscillation of the container's bottom wall is neglected. The contours of the lower boundary at typical timings are illustrated by thick solid lines. The broken lines describe the positions of the layer that are in contact with the container wall. The regions marked by "A" and "B" correspond to the main arches and sub arches, respectively. (b) Space–time diagram of the Type-III undulation corresponding to the one described in Fig. 8 ($L = 140$ mm, $f = 39$ Hz, $a = 1.17$ mm). Main arches and sub-arches are denoted by "A" and "B", respectively, which alternate periodically both in space and time. In the region denoted by "C", the void space between the grains and the space below the arches is indistinguishable in our experiment.

undulation is n (n being an integer or a half integer), is generated for larger external forcing f and/or a under a given size container.

(ii) In contrast to the buckling of the continuum plate, where the wavelength should be equal to L/n (n being an integer or a half integer), the eigenmode conditions are relaxed in the granular layer. Adjustment of the wavelength to the container size is made by the emergence of the solidified parts of the layer or the formation of sub-arches, which play the role of effective side-boundaries for the main arches.

(iii) As far as the near eigenmode is concerned, the wavelength of the undulation (of the fixed thickness layer of the same material) is almost the same for the same value of fa, irrespective of the container size.

(iv) With the increase of the external forcing, the adjustment of the layer in a certain eigenmode U_n (n being an integer or a half integer) becomes no longer attainable, and the transition to the mode $U_{n+1/2}$ occurs.

(v) In the case of near eigenmodes of the vertically vibrated granular layer, the aspect ratio δ/λ of the undulation is one of the appropriate quantities to characterize the arch structure. A similarity relation is found between δ/λ and the forcing fa. Reasonable agreement of the linear fitting of the near eigenmodes with a common slope and an intercept is obtained irrespective of the container size.

4. Discussion

Our experiments were performed using only one species of particles filled in a container up to a certain fixed thickness, so that it is not clear how the slope and the intercept of Eq. (3) depend on the properties of the particle, such as the size d, density ρ, restitution coefficient e, surface roughness or friction, nor how they depend on the layer thickness h or the number of layers $N(\approx h/d)$. Our previous studies [17–19], however, suggest the essential role of the momentum transfer due to the impact of the layer with the container wall on the pattern formation, i.e. the momentum given in the vertical direction induces the vertical compaction and horizontal dilatancy in the granular layer, which causes the buckling of the layer.

According to the theory of elasticity (see, e.g., Ref. [28]), the deformation of the elastic plate of length L, width W and height h, is described by the equation

$$\frac{\mathrm{d}^2\theta}{\mathrm{d}s^2} = -\alpha^2 \sin\theta \tag{4}$$

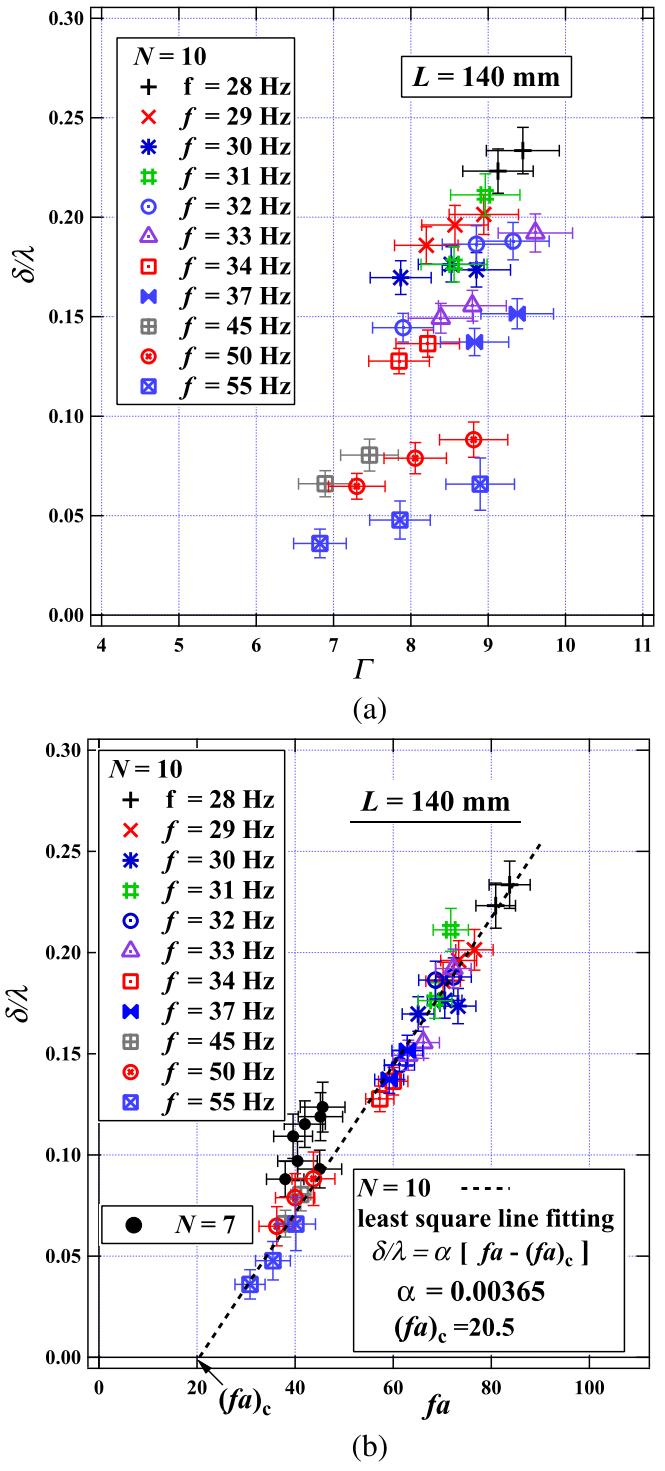

Fig. 14. Dependence of the normalized maximum displacement of arch δ/λ on (a) Γ, and (b) fa. The dotted line in the latter is the least square fit given by Eq. (2).

where θ is the angle tangent to the arc measured from the horizontal direction (x direction), s is the length along the layer measured from one of its end, $\alpha = \sqrt{F_x/E^*I}$, F_x is the force applied horizontally at both ends of the layer, E^* is the effective Young's modulus of the granular layer in the x direction, and $I(\equiv Wh^3/12)$ is the geometric moment of inertia of the cross-sectional area. By applying the boundary condition that the layer meets perpendicularly to the side walls of

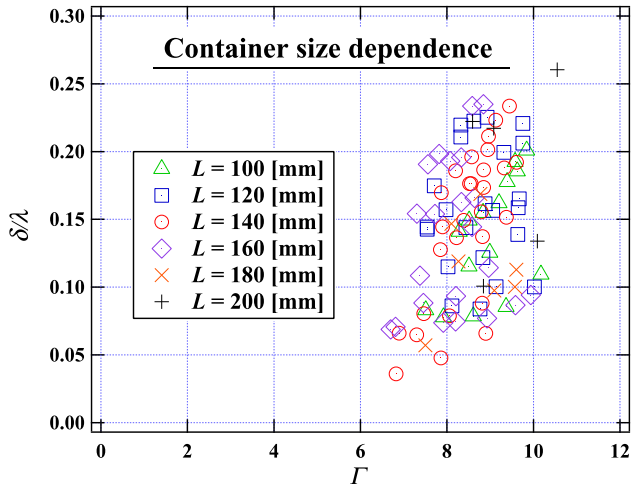

(a)

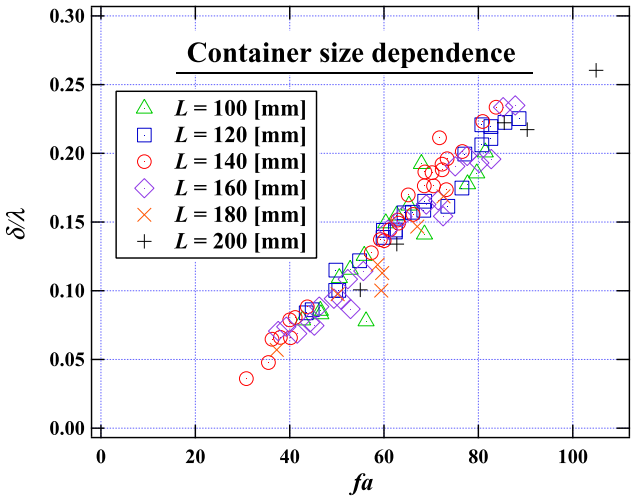

(b)

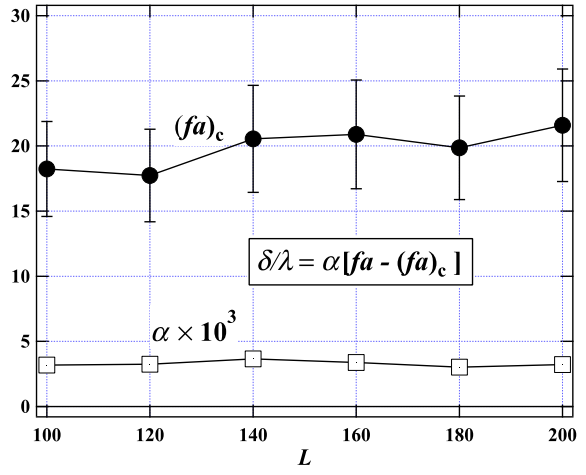

(c)

Fig. 15. Dependence of the container size on the aspect ratio of undulation: (a) δ/λ vs. Γ, (b) δ/λ vs. fa, and (c) the slopes and critical values of Eq. (3) for various container sizes L.

the container, the solution to Eq. (4) admits a particular eigenmode of undulation, whose form is described in terms of the elliptic functions [26]. Based on that theory, the aspect ratio of the wave height δ to wavelength λ is

$$\frac{\delta}{\lambda} = \frac{k}{2E - K} \tag{5}$$

where $K(k)$ and $E(k)$ are the complete elliptic integrals of the first and second kind, respectively, and k is the parameter adjusted at a certain position of the layer. When the initial flat layer of length L is undulated to form the arch, the amount of elongated layer δL is calculated to be

$$\frac{\delta L}{L} = \frac{2(K - E)}{2E - K} \tag{6}$$

For smaller k, Eq. (6) is approximated by

$$\frac{\delta L}{L} = k^2 \left(1 + \frac{9}{8}k^2 + \cdots\right)$$

so that the otherwise flat layer is acted by the force F_x immediately before the buckling:

$$F_x = E^*(Wh)\frac{\delta L}{L} \approx E^* W h k^2 \tag{7}$$

As is mentioned above, the latter force originates in the collision of the layer with the container's bottom wall, which needs some caution. Our observation reveals that (i) the layer meets the bottom of the container at a certain time t_0 when the latter is nearly at the lowest position, (ii) it is pushed up with the container, and then (iii) it is released at a time t_1 when the latter is nearly at the highest upward velocity. This implies that $t_1 \approx t_0 + 1/(4f)$, so that the collision time $\Delta t \approx 1/(4f)$. In a stationary state of undulation, however, it is not the whole layer that collides with the bottom wall at an instance of impact, so that we should consider the effective length of the layer L^* for the estimation of momentum transfer. We shall denote the ratio of L^* to the total layer length L by r. Then the force F_z applied to the layer vertically is roughly estimated by $F_z \sim M^* \Delta v/\Delta t$. Here, $M^* (= r\rho LWh)$ is the relevant mass of the layer, ρ is the density of the layer, and Δv is the difference of the particle velocity before and after the collision. In order to estimate L^*, we subtracted two successive images of the layer with a certain time interval (2 ms in this example) apart, where the position of the bottom wall was chosen as a baseline to observe the relative motion of the particles. Fig. 16(a) is an example of the collision of the layer with the container's wall, and Fig. 16(b) shows the subtracted successive images of the layer. The darker parts of the layer in Fig. 16(b) are the regions with no relative particle motion due to the compaction by the collision, from which we can estimate the effective length L^*, and hence the ratio r. Fig. 16(c) shows the relation between r and the amplitude a of the external oscillation for the cases described in Fig. 14. In spite of large error bars, an almost linear dependence of r on a is recognized (i.e. $r = C_1 a$).

The difference in the velocities Δv is estimated to be $\Delta v = 2\pi f a C_2$ with $C_2 = \cos(2\pi f(t_0 + \Delta t)) - \cos(2\pi f t_0)$, the latter being nearly equal to 1. Thus the excess pressure Δp due to this impact becomes

$$\Delta p = \frac{F_z}{LW} = r\rho h \frac{\Delta v}{\Delta t} = 8\pi C_1 C_2 \rho h f^2 a^2 \tag{8}$$

which will exert the force

$$F_x = (-p_0 + \Delta p)hW \tag{9}$$

on the side walls. Here, $p_0 \equiv C_3 \rho g h$ (C_3 being a constant of order unity) is a "static" pressure, which acts outward normal to the side walls irrespective of the external forcing.

By comparing Eq. (7) and Eq. (9), we have

$$k^2 \approx \frac{8\pi C_1 C_2 \rho h}{E^*}[(fa)^2 - C] \tag{10}$$

where

$$C = \frac{C_3 g}{8\pi C_1 C_2}$$

For smaller values of k, the aspect ratio of the undulation mode U_n given by Eq. (5), combined with Eq. (10), is

$$\frac{\delta}{\lambda} = \frac{2}{\pi}k\left(1 + \frac{3}{4}k^2 + \cdots\right) \approx 4\sqrt{\frac{2C_1 C_2 \rho h}{\pi E^*}}\sqrt{(fa)^2 - C} \tag{11}$$

The latter may also be expressed by

$$\frac{\delta}{\lambda} \approx 4\sqrt{\frac{2C_1 C_2 \rho h}{\pi E^*}}[fa - (fa)_c] \tag{12}$$

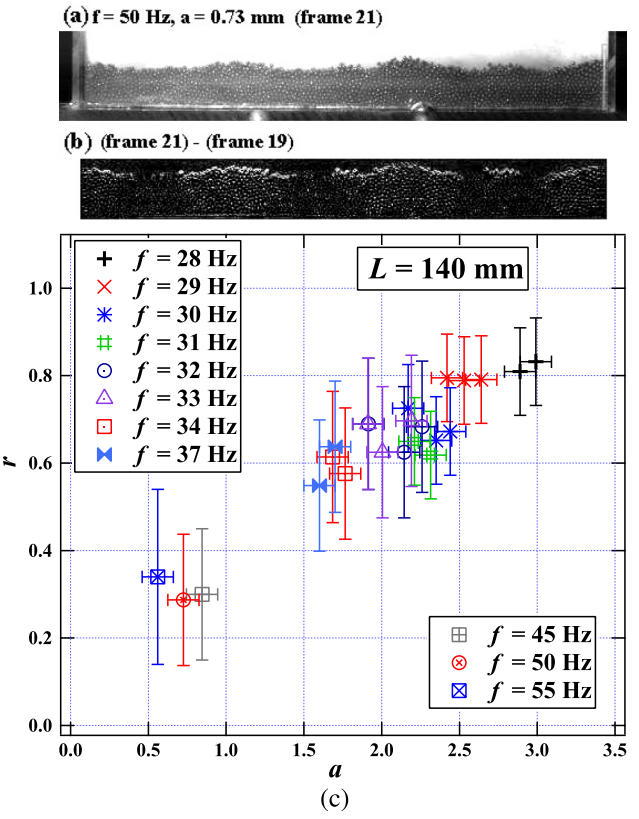

Fig. 16. Partial collision of the layer with the bottom wall: (a) an example of the collision of the layer with the container wall, (b) the subtraction of the successive images of the layer, where the darker parts are the region with no relative motion due to the compaction by the collision, and (c) f and a dependence on the ratio of the compacted length to the total length of the layer.

for larger fa, where

$$(fa)_c = \frac{C}{2fa}$$

Note that the product ρh is constant in the granular layer because of the conservation of the number of particles (and hence the total mass of the layer) confined in a container with fixed L and W. The functional forms of Eq. (11) (i.e., $y = \sqrt{x^2 - C}$) and Eq. (12) (i.e., $y = x - D/x$), are shown in Fig. 17, where C and $D = C/2$ are varied between 10 to 1000, taking into account that $g/(8\pi) \approx 390$ and C_i $(i = 1, 2, 3)$ are of the order of unity. The abscissa x is fa, and the relevant range of x is the one for $y \geq 0$. Except the region very close to $y = 0$, an almost linear relation is recognized, so that Eq. (11) or Eq. (12) reasonably explains our experimental results on the aspect ratio δ/λ.

The above relation also implies the independence of δ/λ on the container size, and the independence of the slope of the fitting line on the layer thickness h (or the number of layer $N \approx h/d$). In Fig. 14(b), we have additionally plotted the similar data obtained for $N = 7$, which were reproduced from our previous papers [24–26]. In spite of larger error bars, the slope for the $N = 7$ case looks almost the same as that for the $N = 10$ case, in qualitative agreement with our theory.

The aspect ratio of the deformation of an elastic plate due to the force F applied normally to both ends is described by

$$\frac{\delta}{\lambda} \propto \sqrt{F - F_c} \tag{13}$$

near the onset of buckling, where F_c is the critical value of F. If we assume that the collision occurs uniformly over the layer and that the collision time Δt is constant, then $F \propto fa$, so that Eq. (13) becomes

$$\frac{\delta}{\lambda} \propto \sqrt{fa - (fa)_c} \tag{14}$$

which is in remarkable contrast to Eq. (11) or Eq. (12). The functional dependence of the latters, therefore, stems from the characteristic behavior of the vibrating granular layer, in which space–time dependent collision processes play important roles. The details, however, are not completely clear, because Eq. (11) and/or Eq. (12) is based on the static theory of buckling, and the quantity E^* and the constants C_i $(i = 1, 2, 3)$ may also depend on the external forcing, which should be clarified in our future study.

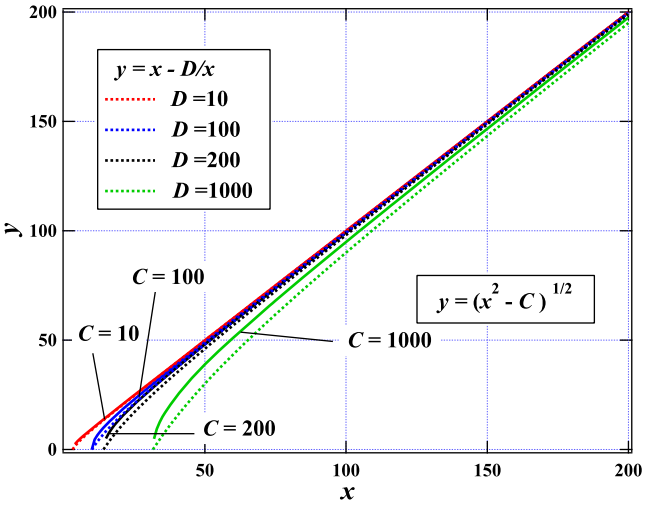

Fig. 17. Functional forms of Eq. (11) and Eq. (12).

Acknowledgements

This work is partially supported by a Grant-in-Aid for Scientific Research (C) from the Ministry of Education, Culture, Sports, Science and Technology, Japan.

References

[1] M. Faraday, On a peculiar class of acoustical figures; and on certain forms assumed by groups of particles upon vibrating elastic surfaces, Philos. Trans. R. Soc. Lond. 121 (1831) 299.
[2] H.M. Jaeger, S.R. Nagel, Physics of the granular state, Science 255 (1992) 1523.
[3] H.M. Jaeger, S.R. Nagel, R.P. Behringer, Granular solids, liquids, and gases, Rev. Mod. Phys. 68 (1996) 1259.
[4] M.C. Cross, P.C. Hohenberg, Pattern formation outside of equilibrium, Rev. Mod. Phys. 65 (1993) 851.
[5] I.S. Aranson, L.S. Tsimring, Patterns and collective behavior in granular media: theoretical concept, Rev. Mod. Phys. 78 (2006) 641.
[6] F. Melo, P. Umbanhowar, H.L. Swinney, Transition to parametric wave patterns in a vertically oscillated granular layer, Phys. Rev. Lett. 72 (1994) 172–175.
[7] F. Melo, P.B. Umbanhowar, H.L. Swinney, Hexagons, kinks, and disorder in oscillated granular layers, Phys. Rev. Lett. 75 (1995) 3838–3841.
[8] P.B. Umbanhowar, F. Melo, H.L. Swinney, Localized excitations in a vertically vibrated granular layer, Nature 382 (1996) 793–796.
[9] T.H. Metcalf, J.B. Knight, H. Jaeger, Standing wave patterns in shallow beds of vibrated granular material, Physica A 236 (1997) 202–210.
[10] C. Bizon, M.D. Shattuck, J.B. Swift, W.D. McCormick, H.L. Swinney, Patterns in 3D vertically oscillated granular layers: simulation and experiment, Phys. Rev. Lett. 80 (1998) 57–60.
[11] O. Sano, A. Ugawa, K. Suzuki, Pattern formation on the vertically vibrated granular layer, Forma 14 (1999) 321–329.
[12] P.B. Umbanhowar, H.L. Swinney, Wavelength scaling and square/stripe and grain mobility transitions in vertically oscillated granular layers, Physica A 288 (2000) 344–362.
[13] E. Clément, L. Vanel, J. Rajchenbach, J. Duran, Pattern formation in a vibrated granular layer, Phys. Rev. E 53 (1996) 2972–2975.
[14] K.M. Aoki, T. Akiyama, Spontaneous wave pattern formation in vibrated granular materials, Phys. Rev. Lett. 77 (1996) 4166–4169.
[15] A. Ugawa, O. Sano, Dispersion relation of standing waves on a vertically oscillated thin granular layer, J. Phys. Soc. Jpn. 71 (2002) 2815–2819.
[16] O. Sano, Solid–fluid transition and the formation of ripples in vertically oscillated granular layers, AIP Conf. Proc. 1227 (2010) 100–114.
[17] O. Sano, Density wave as a mechanism of the formation of ripples in vertically oscillated granular layer, J. Phys. Soc. Jpn. 80 (2011) 034402.
[18] O. Sano, Wavelength selection mechanism of ripples in vertically vibrated thicker granular layer, J. Phys. Soc. Jpn. 81 (2012) 033401.
[19] O. Sano, Wavelength selection of ripples in vertically vibrating dynamically thick granular layer due to density wave refraction, C. R. Mecanique 342 (2014) 52–62.
[20] S. Douady, S. Fauve, C. Laroche, Subharmonic instabilities and defects in a granular layer under vertical vibrations, Europhys. Lett. 8 (1989) 621–627.
[21] A. Goldshtein, M. Shapiro, L. Moldavsky, M. Fichman, Mechanics of collisional motion of granular materials. Part 2. Wave propagation through vibrofluidized granular layers, J. Fluid Mech. 287 (1995) 349–382.
[22] Y. Lan, A.D. Rosato, Convection related phenomena in granular dynamics simulations of vibrated beds, Phys. Fluids 9 (1997) 3615–3624.
[23] S.-J. Moon, M.D. Shattuck, C. Bizon, D.I. Goldman, J.B. Swift, H.L. Swinney, Phase bubbles and spatiotemporal chaos in granular patterns, Phys. Rev. E 65 (2002) 011301.
[24] A. Ugawa, O. Sano, Undulation of a thin granular layer induced by vertical vibration, J. Phys. Soc. Jpn. 72 (2003) 1390–1395.
[25] K. Kanai, A. Ugawa, O. Sano, Experiment on vibration-induced pattern formation of a vertically thin granular layer, J. Phys. Soc. Jpn. 74 (2005) 1457–1463.
[26] O. Sano, Dilatancy, buckling, and undulations on a vertically vibrating granular layer, Phys. Rev. E 72 (2005) 051302.
[27] A. Götzendorfer, C.-H. Tai, C.A. Kruelle, I. Rehberg, S.-S. Hsiau, Fluidization of a vertically vibrated two-dimensional hard sphere packing: a granular meltdown, Phys. Rev. E 74 (2006) 011304.
[28] L.D. Landau, E.M. Lifshitz, Theory of Elasticity, Pergamon, Oxford, 1986.